Experimental Thermal and Fluid Science 120 (2021) 110178

Contents lists available at ScienceDirect

Experimental Thermal and Fluid Science

journal homepage: www.elsevier.com/locate/etfs

From sparse data to high-resolution fields: ensemble particle modes as a basis for high-resolution flow characterization

J. Cortina-Fernández, C. Sanmiguel Vila, A. Ianiro, S. Discetti*

Aerospace Engineering Research Group, Universidad Carlos III de Madrid, Leganés, Spain

ARTICLE INFO

Keywords:
Proper orthogonal decomposition
Particle tracking
Flow measurements

ABSTRACT

In this work, we present an approach to reconstruct high-resolution flow velocity or scalar fields from sparse particle-based measurements such as particle tracking velocimetry, thermographic phosphors or pressure-sensitive particles. The proposed approach can be applied to any of those fields; without leading its generality, it is hereby assessed for flow velocity measurements. Particles allow probing physical quantities at multiple time instants in randomly located points in the investigated region. In previous works, it has been shown that high-resolution time-averaged fields can be estimated by an ensemble average of the particles contained into spatial bins whose size can be reduced almost *ad libitum*. In this work, high-resolution *ensemble particle modes* are estimated from the ensemble average of particles, weighted with Proper Orthogonal Decomposition time coefficients which are estimated from low-resolution spatially-averaged fields. These modes represent a self-tunable compressed-sensing library for the reconstruction of high-resolution fields. High-resolution instantaneous fields are then obtained from a linear combination of these modes times their respective time coefficients. This data-enhanced particle approach is assessed employing two DNS datasets: the wake of a cylinder and a fluidic pinball. It is shown here that it is possible to reconstruct phenomena whose characteristic wavelength is smaller than the mean particle spacing whenever such events are correlated with any other flow phenomenon with a wavelength large enough to be sampled. The proposed approach is also applied to experimental wind-tunnel data, again showing excellent performances in presence of realistic measurement-noise conditions.

1. Introduction

Seeding particles allow probing scalar and vector quantities in a flow providing insightful spatial information both about velocity fields -employing techniques such as the now widespread Particle Image Velocimetry (PIV) [1,2]- and scalar quantities such as temperature or pressure [3,4].

However, the characterization of turbulent flows is extremely demanding due to the large range of scales involved. A typical figure of merit is the Dynamic Spatial Range (DSR), defined as the ratio between the largest and the smallest measurable scale in a flow [5]. Recently, a generalized definition has been proposed [6], in which the smallest measurable scale is equal to the interrogation-window size in cross-correlation algorithms, or is a function of the average inter-particle distance in Particle Tracking Velocimetry (PTV). In all cases, supposing a typical interrogation-window size of 32 pixels (which is a good compromise between the desire of a high resolution and an acceptable level of noise), the DSR is of the order of $0.03L$ in planar PIV, where L is the linear sensor size in pixels. In 3D velocimetry, due to the need of reconstructing a particle distribution in a volume, the scaling with the sensor length is even less than linear. However, spatial scales in turbulent flows have a wide spectrum, being the ratio between integral and Kolmogorov scale proportional to $Re^{3/4}$ [7], where Re is the Reynolds number based on the large-scale size and velocity. The need of satisfying this requirement has motivated intense efforts to improve the measurement DSR in the last 20 years. Most recent advances in 3D PTV (see for instance the results of the 3D test cases of the 4^{th} International PIV Challenge [8]) are demonstrating superior performances of particle-tracking approaches. Nonetheless, it is needed a radical change of approach to go beyond the limit set by the average inter-particle spacing.

DSR limitations have been easily overcome for turbulent statistics with ensemble-correlation [9,10] and ensemble-particle-averaging [11–13] approaches. Ensemble-particle averaging has widely demonstrated superior performances [12,14] than cross-correlation-based techniques. Ensemble PTV is based on generating dense velocity-vector distributions using data from different snapshots, and binning the cloud of vectors to locally extract turbulent statistics. The ensemble PTV

* Corresponding author.
E-mail address: sdiscett@ing.uc3m.es (S. Discetti).

https://doi.org/10.1016/j.expthermflusci.2020.110178
Received 8 January 2020; Received in revised form 7 April 2020; Accepted 19 May 2020
Available online 29 May 2020
0894-1777/

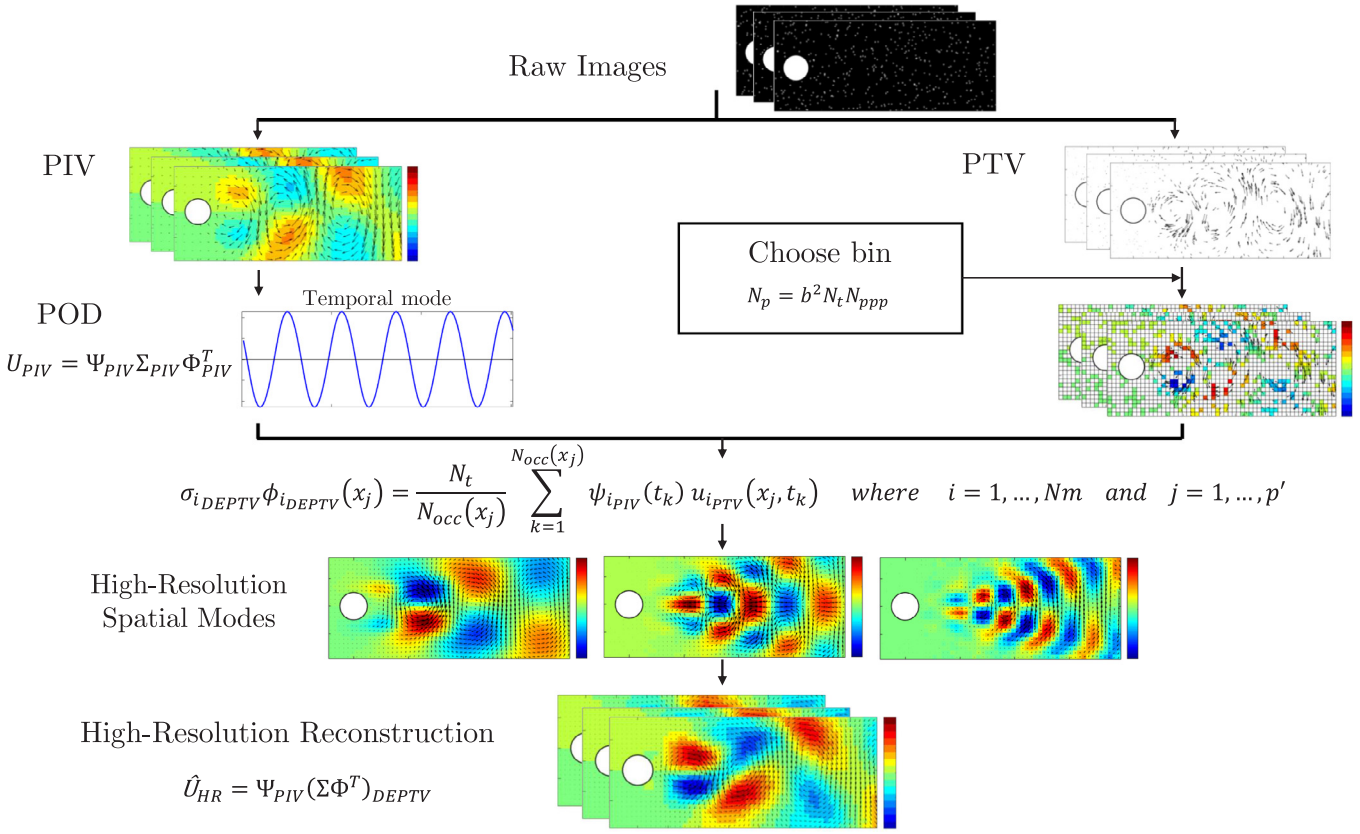

Fig. 1. Flowchart of the proposed Data-Enhanced PTV.

approach exploits the ergodicity of the flow obtaining time-average and flow statistics among the available samples in each bin and does not require that samples at each bin are recorded simultaneously. Despite employing very sparse datasets (in which the particle image concentration can be well below 0.05 particles per pixel), the ensemble approach allows increasing almost *ad libitum* the DSR of turbulent statistics, employing a sufficiently-large number of snapshots. In fact, as shown by Kähler et al. [12], the bound of the root-mean-square error of the particle-center detection results in a sub-pixel resolution limit for the ensemble PTV.

When dealing with instantaneous fields, however, PTV provides velocity measurements only in the spatial locations in which particles are available, resulting in a sparse sampling of the velocity field. If we consider the most intuitive approach of re-interpolating the velocity fields on a structured grid, the instantaneous-field resolution is bound to the particle sampling of the instantaneous fields, i.e. to the spacing between the particles. Nevertheless, if a *dictionary* of flow structures were available, the gaps between velocity vectors could be filled in the instantaneous fields in the same way a contestant would solve the word puzzles in the TV show *Wheel of Fortune*.

Gappy fields are usually completed employing kriging [15] or Proper Orthogonal Decomposition (POD) approaches [16]. Probably the best results over gappy data have been obtained with approaches such as the *marred faces* reconstruction [16] or the gappy-POD filling procedures [17,18]. In these works, gappy fields are seen as snapshot vectors with zero values in correspondence of the gaps. The gappy fields are employed to estimate non-gappy modes of the flow field which are then linearly combined using a temporal basis to obtain the instantaneous fields with no gaps. In the work by Everson and Sirovich [16], the temporal basis is estimated directly by carrying out a proper orthogonal decomposition of the gappy data, while Venturi and Karniadakis [17] proposed to adjust it iteratively by progressively adding modes and thus filling the gaps. It has to be remarked here that using the full set of modes would return the original gappy dataset; for this purpose, Raben et al. [18] proposed a criterion based on data smoothness for the choice of the number of modes to be employed to fill the gaps. The stopping method relies on the regularized spatial basis of PIV or of PTV data interpolated on a Eulerian grid, thus not requiring an iterative procedure. However such methods have demonstrated to be successful in turbulent environments [19] only for relatively-low gappyness levels.

Merging the ideas of gappy POD and of ensemble-particle-averaging approaches, the method proposed here aims at reconstructing high-resolution instantaneous fields as a linear combination of high-resolution modes, referred to as *ensemble particle modes*. These modes are estimated from the ensemble average of particles, weighted with POD time coefficients which are computed from low-resolution spatially-averaged fields. The ensemble particle modes represent a self-tunable dictionary for the compressed sensing of the high-resolution flow fields. The whole learning procedure is unsupervised, with minimal input from the user and is named here *Data-Enhanced Particle Tracking Velocimetry* (from now on DEPTV).

The method is outlined in Section 2. A validation (Section 3) is carried out with steps of increasing complexity. The first test case is the wake of a cylinder at $Re = 100$ (Section 3.1), with velocity vectors directly extracted from a DNS database. The second test case (Section 3.2) is the wake of the fluidic pinball [20,21], i.e. an arrangement of three cylinders whose centres form an equilateral triangle. For this test case, virtual images are generated, thus introducing also effects of noise contamination due to particle-localization uncertainty. The DEPTV is finally assessed against an experimental test case in Section 4. The experiment consists of the measurement of the wake of two cylinders with different diameters, one being sufficiently large to be adequately discretized by standard cross-correlation-based PIV, and the second one with a diameter of the order of the interrogation-window size, which clearly challenges the resolution limits of PIV algorithms.

2. Algorithm description

The proposed algorithm is outlined in the flow chart of Fig. 1. The resolution enhancement is achieved through the calculation of spatial modes with a resolution higher than that of the PIV snapshots (i.e. with grid elements, from now on *bins*, smaller than the PIV interrogation window). The high-resolution spatial modes are calculated from the ensemble averaging into small bins of the PTV vectors from the whole dataset, weighted with an appropriate temporal basis.

First of all, the images undergo a "traditional" processing step. Data on an Eulerian grid are obtained using either a standard cross-correlation-based PIV analysis on the raw images or interpolating PTV data onto a fixed grid. The fluctuating part $\mathbf{u} = [u, v, w]$ of the velocity field $\mathbf{U} = [U, V, W]$ is stored in the form of the snapshot matrix $\boldsymbol{U}_{PIV} \in \mathbb{R}^{N_t \times p}$, with N_t being the number of snapshots and p being the number of grid points. Then, following the snapshot implementation [22], POD is carried out to obtain the decomposition basis in space, $\boldsymbol{\Phi}_{PIV}$, and time, $\boldsymbol{\Psi}_{PIV}$.

$$\boldsymbol{U}_{PIV} = \boldsymbol{\Psi}_{PIV}\, \boldsymbol{\Sigma}_{PIV}\, \boldsymbol{\Phi}_{PIV}^{T} \tag{1}$$

The same images are then analyzed with a PTV algorithm to identify particle pairs for each snapshot. This data will be the basis to obtain high-resolution *ensemble particle modes* on a structured grid. Such grid is defined within the space domain, and each grid point corresponds to a bin and collects the PTV data of the particles that lie within each bin.

The high-resolution spatial modes are calculated by projecting the PTV data $\boldsymbol{U}_{PTV}$ on the PIV temporal basis $\boldsymbol{\Psi}_{PIV}$. The data matrix $\boldsymbol{U}_{PTV}$ can be formally approximated as the Hadamard product of the unknown high-resolution velocity field $\boldsymbol{U}_{HR}$ times a Dirac delta function matrix, with zeros entries in the locations with no velocity information:

$$\boldsymbol{U}_{PTV} = \boldsymbol{\delta} \odot \boldsymbol{U}_{HR} \tag{2}$$

To account for the sparsity of $\boldsymbol{U}_{PTV}$, ensemble particle modes are obtained as a weighted average of PTV vectors (projected on the POD temporal basis from PIV) in each bin. The following expression is used to estimate the ensemble particle modes $\sigma_{iDEPTV}\, \boldsymbol{\phi}_{iDEPTV}$ to account for the different number of data points per bin (referred to as occurrences):

$$\sigma_{iDEPTV}\, \phi_{iDEPTV}(x_j) = \frac{N_t}{N_{occ}(x_j)} \sum_{k=1}^{N_{occ}(x_j)} \psi_{iPIV}(t_k)\, u_{iPTV}(x_j,\, t_k)$$
$$i = 1, \ldots, N_m \quad j = 1, \ldots, p' \tag{3}$$

where $N_{occ}(x_j)$ is the number of occurrences per bin, p' is the number of grid points of evaluation, ϕ_{iDEPTV} is the i^{th} "unitary-norm" ensemble particle mode and σ_{iDEPTV} is its corresponding norm.

In matrix form, Eq. (3) reads as:

$$(\boldsymbol{\Sigma}\boldsymbol{\Phi}^{T})_{DEPTV} = \widehat{\boldsymbol{N}} \odot \boldsymbol{\Psi}_{PIV}^{T}\, \boldsymbol{U}_{PTV} \tag{4}$$

where $\widehat{\boldsymbol{N}} \in \mathbb{R}^{N_m \times p'}$. The rows of $\widehat{\boldsymbol{N}}$ contain the scaling factors $N_t/N_{occ}(x_j)$ to account for the sparsity of the bins, i.e. not all bins contribute N_t-times to the product in Eq. (3).

The achievable size b of the bins (supposed square for simplicity) depends on the desired number of particles required to achieve sufficient statistical convergence. It can be determined by:

$$b = \sqrt{\frac{N_p}{N_t \cdot N_{ppp}}} \tag{5}$$

where N_p is the desired number of particles per bin, N_t is the number of snapshots and N_{ppp} is the particle image density, expressed in particles per pixel. As evident from Eq. 5 the bin size can be decreased (and thus the spatial resolution of the ensemble particle modes can be increased) *ad libitum*, down to the spatial resolution limit of ensemble PTV, by increasing the number of snapshots.

A low-order reconstruction of the instantaneous velocity field is performed using the highly-resolved POD modes of the PTV data and the PIV temporal modes to compute high-resolution velocity fields. The estimated high-resolution snapshot matrix $\widehat{\boldsymbol{U}}_{HR}$ is:

$$\widehat{\boldsymbol{U}}_{HR} = \boldsymbol{\Psi}_{PIV}\, (\boldsymbol{\Sigma}\boldsymbol{\Phi}^{T})_{DEPTV} \tag{6}$$

where the elements of $(\boldsymbol{\Sigma}\boldsymbol{\Phi}^{T})_{DEPTV}$ are computed according to Eq. (3).

The effects of the presence of the gaps was included in the modal decomposition in none of the above-mentioned algorithm [16–18]. With the weighting factor $N_t/N_{occ}(x_j)$ included in Eq. (3), the energy assigned to each grid point is properly scaled, provided that satisfactory statistical convergence is achieved.

It has to be remarked herein that the high-resolution snapshots are obtained employing the POD temporal basis of the low-resolution fields. Consequently, the present methodology is only able to recover the high-frequency part of the large-scale spatial modes which were already measured (even if modulated in intensity) with the low-resolution PIV.

3. Validation

3.1. DNS of the wake of a cylinder

3.1.1. Database and numerical settings

The first validation test case is from a Direct Numerical Simulation (DNS) of the two-dimensional fluid flow past a cylinder with $Re = 100$. The database was obtained from Ref. [23] (www.dmdbook.com). The original dataset was generated using an Immersed Boundary Projection Method [24,25]. The spatial resolution is 199×449 points, covering a domain of 9×4 diameters D in the ranges $x/D \in [-1, 8]$ and $y/D \in [-2, 2]$ and it contains 151 snapshots. The vortex shedding in the wake is periodic, with a periodicity of 30 snapshots. The contour plot of the fluctuating streamwise velocity component, together with a superimposed vector-arrow representation of the fluctuating velocity field, is reported in Fig. 2.

For this validation, the resolution of the snapshots of the virtual experiments is reduced to 100×225 pixels, i.e. 2 pixels are equivalent to 1 DNS grid point. Pseudo-PIV fields are generated by filtering the DNS data with a top-hat filter of 40×40 pixels. From simplicity of notation, from now on we will refer to it simply as PIV. Data are extracted with a step of 10 pixels, thus simulating PIV fields with an interrogation window of 40×40 pixels and 75% overlap.

The particle image density is fixed to $N_{ppp} = 0.02$ particles per pixel, with mean particle spacing of about 7 pixels. The DEPTV grid is set with grid spacing $dx = 4$ pixels, leading to 23×55 vectors. A parametric study is carried out by varying the bin size and the number of particles per bin for each number of snapshots. The bin size has to be tuned depending on the number of images and the number of particles per bin, according to Eq. 5.

3.1.2. High-resolution POD modes

A comparison of the modes 2, 4 and 6 of the streamwise velocity component is displayed in Fig. 3. The spatial modes of the DNS are

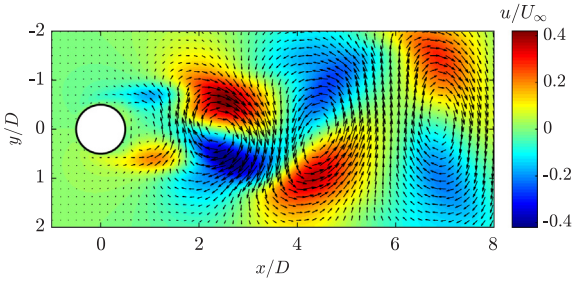

Fig. 2. Original snapshot from the DNS database of the wake of a cylinder at $Re = 100$ [23]. Contour of the fluctuating part of the streamwise velocity components, superposed with vector arrows of fluctuating velocity. Velocities are referenced to the free stream velocity.

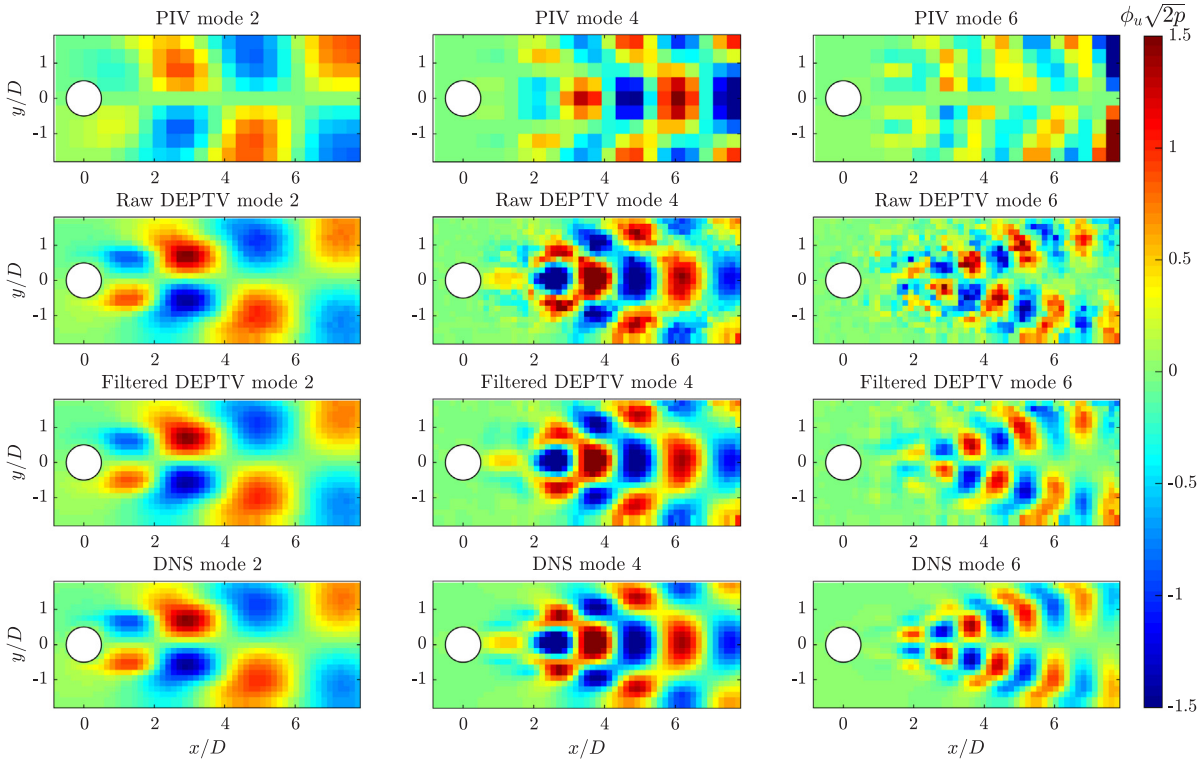

Fig. 3. Comparison of the POD spatial modes 2, 4 and 6. From the top row to the bottom: PIV; Data-Enhanced PTV; Data-Enhanced PTV after polynomial smoothing; DNS spatial modes obtained after projection on the PIV temporal base $\boldsymbol{\Psi}_{PIV}$. For the DEPTV the following parameters have been set: $N_p = 800$, $N_t = 1510$ and bin size of 5.1 pixels.

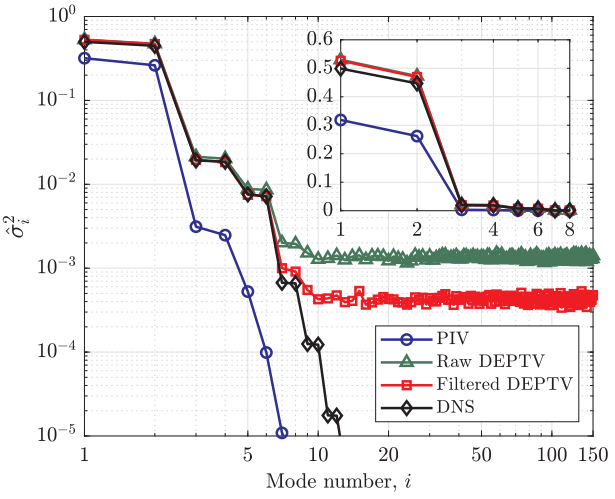

Fig. 4. Singular value distribution of the PIV snapshots and the original DNS database, superposed with the norm of the extended POD modes with and without polynomial filtering. For the DEPTV the following parameters have been set: $N_p = 800$, $N_t = 1510$, $b = 5.1$ pixels. The singular values are normalized with the sum of the singular values of the DNS case, and scaled to account for the number of grid points as in Eq. 7. Inset figure displays the distribution of the first 8 modes in a linear vertical scale.

obtained by projection on the PIV temporal basis $\boldsymbol{\Psi}_{PIV}$ to provide a direct comparison with PIV and ensemble particle modes; for the same purpose the modes are multiplied by the square root of the number of grid points so that they have unitary norm when integrated over the area. The modes obtained as the projection of the DNS fields on the PIV temporal basis are referred to as extended POD modes, following Ref. [26]. The mode 2 of PIV can identify the fluctuations due to the wake shedding (which is largely modelled by the first two modes as a travelling wave), but with evident spatial filtering issues if compared to the DNS spatial mode. In mode 4 a higher-order harmonic is identified, even though also in this case smoothing is evident in the near field. The structure of mode 6 from standard PIV is completely distorted, since it involves scales smaller than the PIV interrogation window.

The second row of Fig. 3 reports the spatial modes obtained through the proposed Data-Enhanced PTV, setting 800 particles per bin on a set of 1510 images, thus corresponding to a bin size of 5.1 pixels according to Eq. 5. In this case the bin size is smaller than the average particle distance, and it corresponds to approximately a 50% gappyness level in each snapshot (i.e. each bin contains on average about 0.5 particles per snapshot). DEPTV can recover also the flow organization close to the cylinder in both modes 2 and 4. It is worth highlighting that this is a perfect example of high-frequency content which is recovered with the present methodology, starting from a large-wavelength mode. Mode 6 resembles quite clearly the pattern observed in the extended DNS modes, even though contaminated by noise. For this reason, a data smoothing with a Savitzky-Golay filter of the 2^{nd} order is proposed. This filter has already been introduced in the Ensemble PTV algorithms to reduce the effects of poor resolution due to finite bin size on the computation of the Reynolds stresses [13]. The advantage of the application of the Savitzky-Golay filter is that the peaks are reasonably-well preserved, while the random noise is effectively suppressed in POD modes which are expected to be smooth in the majority of incompressible flow PIV measurements. The filtered DEPTV modes of the third row of Fig. 3 are the basis for the low-order reconstruction of high-resolution velocity fields.

The singular values of the PIV snapshot matrix are displayed in Fig. 4 for the same case of $N_t = 1510$. The norm of the extended POD [26] modes obtained from the DNS database by projection on the PIV temporal modes, and of the modes obtained by Eq. (3) before and after the application of the Savitzky-Golay filter, are reported for comparison. Without leading the generality, we will refer to these values as the norm of the spatial modes (including the PIV dataset). Indeed, while for

PIV data it can be properly used the nomenclature “singular values”, for the DNS and DEPTV datasets the obtained extended modes are not necessarily sorted by their energy contribution. For a proper comparison, the squared norm of the modes is normalized with the number of grid points to take into account the fact that the datasets are defined on different grids, and are normalized by the sum of the squared singular values computed for the DNS case:

$$\hat{\sigma}_i^2 = \frac{\sigma_i^2}{\sum_{i=1}^{N_{m,DNS}} \sigma_{i,DNS}^2} \frac{p_{DNS}}{p} \tag{7}$$

where $N_{m,DNS}$, $\sigma_{i,DNS}$ and p_{DNS} are respectively the number of modes, singular values and number of grid points of the original DNS database, σ_i and p are the singular values and number of grid points of PIV or DEPTV, depending on the analyzed case, and $\hat{\sigma}_i$ are the normalized singular values.

The scaled norm of the PIV modes has lower intensity than the norm of the extended POD modes of the dataset due to spatial filtering effects of the PIV interrogation window. DEPTV can recover in full this issue for the first 6 modes. Starting from mode 10, while the norm of PIV and DNS modes is rapidly decreasing for increasing mode number, the norm of the ensemble particle modes reaches a substantially stable level. By visual inspection of the modes, it is clear that this plateau corresponds to modes contaminated by noise. The definition of the standard error, for normally-distributed data sets, suggests that the convergence error of the mean and or of the statistics is proportional to the signal standard deviation divided by the square root of the number of samples over which the mean and the statistics are computed [27]. It can thus be hypothesized that higher-order modes which contain a contribution to the total flow variance equal to or smaller than the typical value of $1/\sqrt{N_{occ}}$ are affected by such high level of measurement noise that can not be recovered with the ensemble-particle approach. The flow-field reconstruction is thus carried out by retaining only the first 10 modes, using the plateau of the norm of the DEPTV modes to set the cutoff mode number.

3.1.3. Reconstruction error

Fig. 5 shows the normalized standard deviation of the error of $\widehat{\boldsymbol{U}}_{HR}$ compared with the original dataset as a function of the squared bin size for three different numbers of snapshots. The error is estimated as in Eqs. (8)–(10).

$$\varepsilon_r(x,\, t) = \frac{\sqrt{(\hat{u} - u_{DNS})^2 + (\hat{v} - v_{DNS})^2}}{U_\infty} \tag{8}$$

$$\bar{\varepsilon}_r(x) = \frac{1}{N_t} \sum_{i=1}^{N_t} \varepsilon_r(x,\, t_i) \tag{9}$$

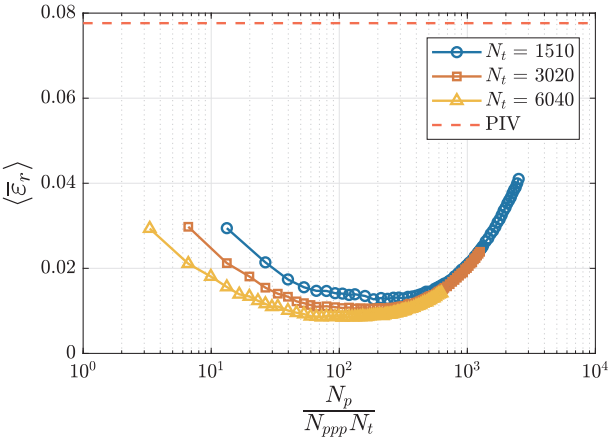

Fig. 5. Error of standard PIV and DEPTV as a function of the square bin size for three different image datasets.

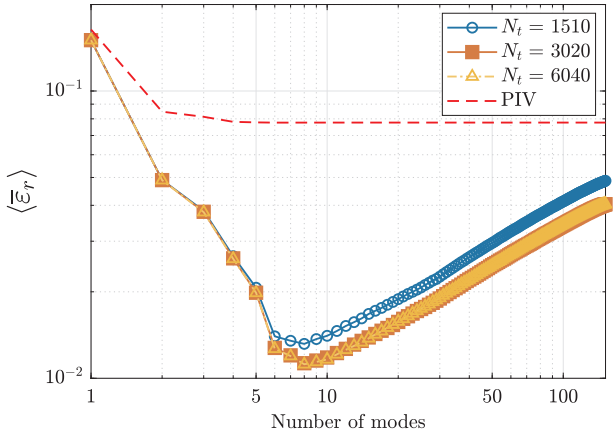

Fig. 6. Error in the flow field as a function of the number of modes. $N_p = 800$. Bin sizes of 5.1, 3.6, 2.6 pixels for $N_t = 1510$, $N_t = 3020$ and $N_t = 6040$ respectively.

$$\langle \bar{\varepsilon}_r \rangle = \frac{1}{p} \sum_{j=1}^{p} \bar{\varepsilon}_r(x_j) \tag{10}$$

Here $\hat{u}$ and $\hat{v}$ are the measured velocity fluctuations in the streamwise and crosswise directions respectively. In all the cases, there is an optimum bin size that minimizes the error. Increasing the bin size with a fixed number of images, the number of occurrences within each bin increases, thus reducing the random error in the estimated modes. On the other hand, increasing the bin size also increases the spatial filtering effects due to finite spatial resolution, thus introducing more significant systematic errors. For a given number of snapshots acquired with a certain particle density, the optimum number of particles (and thus the bin size) is a compromise between these two contributions. Also, in all cases, a significant reduction of the total error with respect to the standard PIV algorithm is observed.

The effect of the cutoff choice on the average error (according to Eqs. (8)–(10)) is presented in Fig. 6. The error is also estimated for the corresponding low-order reconstruction from PIV using an increasing number of modes. The DEPTV-based reconstruction is carried out setting a number of particles per bin equal to 800 and for three different sets of images (N_t = 1510, 3020 and 6040, corresponding respectively to a bin size of 5.1, 3.6 and 2.6 pixels). The inclusion of the most energetic modes reduces rapidly the error up to 8 modes, with a significantly faster rate than the standard PIV. DEPTV is indeed able to achieve better resolution for the most energetic large-scale modes, not only in terms of spatial distribution (Fig. 3) but also in terms of corresponding energy content (Fig. 4). For the case of PIV, the error decreases monotonically until reaching an asymptotic value, which corresponds to the systematic error due to finite spatial resolution. For DEPTV there is an optimum number of modes for the reconstruction, beyond which the poor convergence of the modes is detrimental for the reconstruction accuracy. By comparison between Fig. 4 and Fig. 6, it is clear that this minimum point corresponds to the start of the plateau of the norm of the modes obtained from DEPTV.

Assuming that the noise contained in the ensemble particle modes is due to insufficient statistical convergence, it is expected to be random and uniform among the modes. This hypothesis is in agreement with the mode norm versus mode number reported in Fig. 4 which, after a certain number of modes, becomes practically constant, slowly approaching an asymptotic value. As an empirical criterion for mode truncation in the low-order reconstruction, based on the empirical evidence of present test cases, it is advisable to truncate the reconstruction with the mode whose norm is 20% larger than the asymptotic value.

Finally, a low-order reconstruction of the instantaneous velocity field using 10 modes is displayed in Fig. 7. Contours of the fluctuating

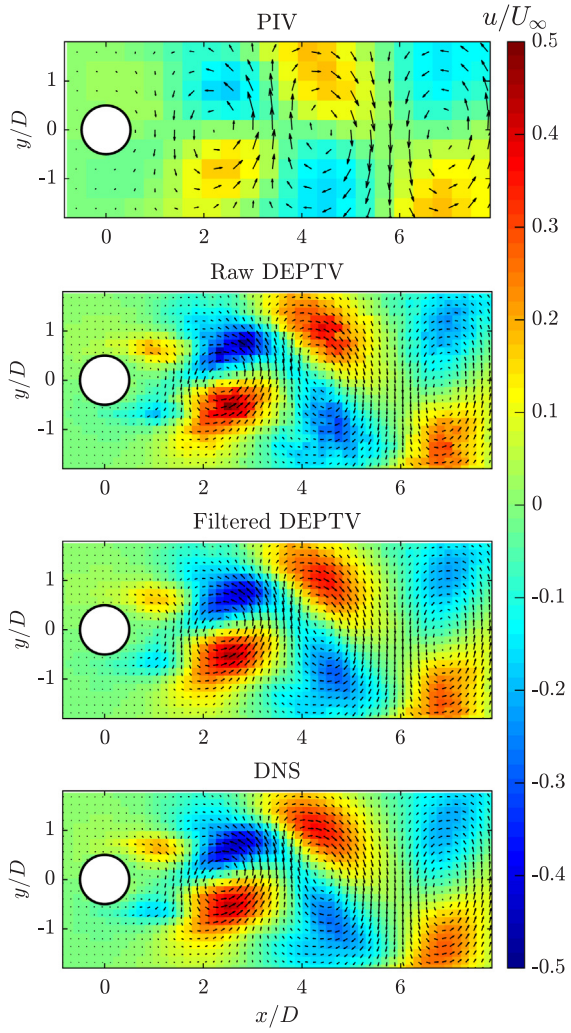

Fig. 7. Comparison of the instantaneous flow field. $N_t = 1510$, $N_p = 800$, $b = 5.1$ pixels.

streamwise velocity component with superposed vector representation of the fluctuating velocity field for PIV and DEPTV are assessed against the original DNS field. The DEPTV reconstruction is reported in this case for $N_t = 1510$, $N_p = 800$ and a corresponding bin size of 5.1 pixels. The proposed DEPTV method can recover the correct intensity of the peaks of the streamwise velocity fluctuations, which were significantly attenuated by the original PIV processing. Additionally, the information in the near-field of the cylinder wake is recovered. The velocity fluctuations in the near wake were completely cancelled by the PIV processing due to spatial-resolution limitations; nonetheless, due to the statistical correlation of the near field region with the developing wake, the temporal basis obtained from the POD of the PIV fields is a sufficient input to recover it with the proposed DEPTV approach.

3.2. Fluidic pinball

3.2.1. Database and numerical settings

The second test case is the flow in the wake of a set of three cylinders with equal radius $R = D/2$, whose centres form an equilateral triangle with side length equal to $3R$. The triangle is oriented with an upstream vertex and with the downstream side orthogonal to the freestream flow, located at $x = 0$ and centred with respect to the y axis. This configuration, referred as *fluidic pinball* [21], is an extremely interesting test case for flow-control applications. For the purpose of this

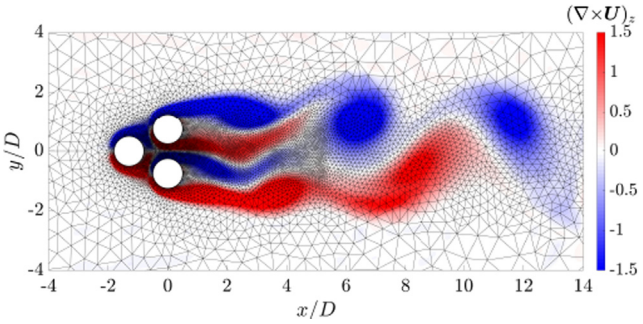

Fig. 8. Original snapshot of the fluidic pinball DNS database. Contour of the out-of-plane vorticity, superposed on the DNS mesh.

work, the wake of the pinball provides additional challenges to the previous test case, with the interaction of the wakes of three bodies, a region of development and the final merging in a large-scale unique shedding wake. DNS data at $Re = 130$ (referred as chaotic regime [21]) are used to generate synthetic PIV images. The details of the simulation settings and flow behaviour can be found in Refs. [20,21,28]. An example of a snapshot is presented in Fig. 8, with the contour of the instantaneous out-of-plane vorticity and superposed computational mesh.

Differently from the previous case, here synthetic PIV images are generated with a custom-made code. Gaussian blobs with a maximum intensity of 100 counts and 2.5 pixels diameter are generated on 8-bit images. A total of 5000 snapshots has been generated; since the flow is periodic with a period of approximately 100 snapshots, this corresponds to 50 periods. The flow field covers the range $x/D \in [-5D, 15D]$ in the streamwise direction and $y/D \in [-5D, 5D]$ in the crosswise direction, with a resolution of 25 pixels/D.

The images are processed with a custom-made multi-pass [29] image deformation [30] PIV algorithm developed at the University of Naples [31]. The interrogation window is set to 40 × 40 pixels with 75% overlap. Particle Tracking is carried out with a super-resolution approach [32], i.e. the PIV fields are used as a predictor to identify particle image pairs.

3.2.2. High-resolution POD modes

The singular values of the original dataset and the PIV are reported in Fig. 9. For this purpose, the DNS data are interpolated on a regular grid with spacing equal to 4 pixels. The norms of the extended modes with the proposed DEPTV before and after smoothing with the Savitzky-Golay filter are included for comparison. The data are presented

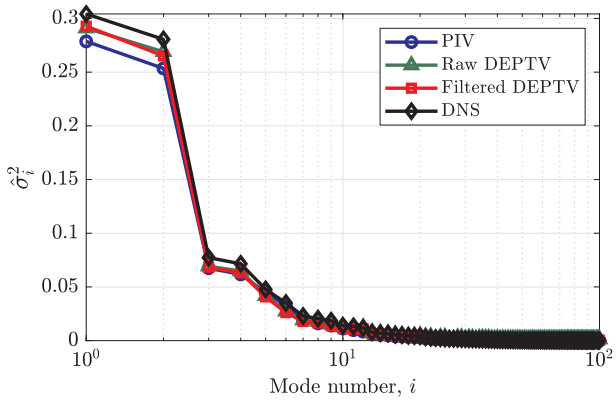

Fig. 9. Singular values distribution of the PIV snapshots and the original DNS database, superposed with the norm of the ensemble particle modes with and without polynomial filtering, for the fluidic pinball test case. $N_{ppp} = 0.01$, $b = 4$ pixels, $N_t = 5000$. The singular values are normalized with the sum of the singular values of the DNS case, and scaled to account for the number of grid points as in Eq. 7.

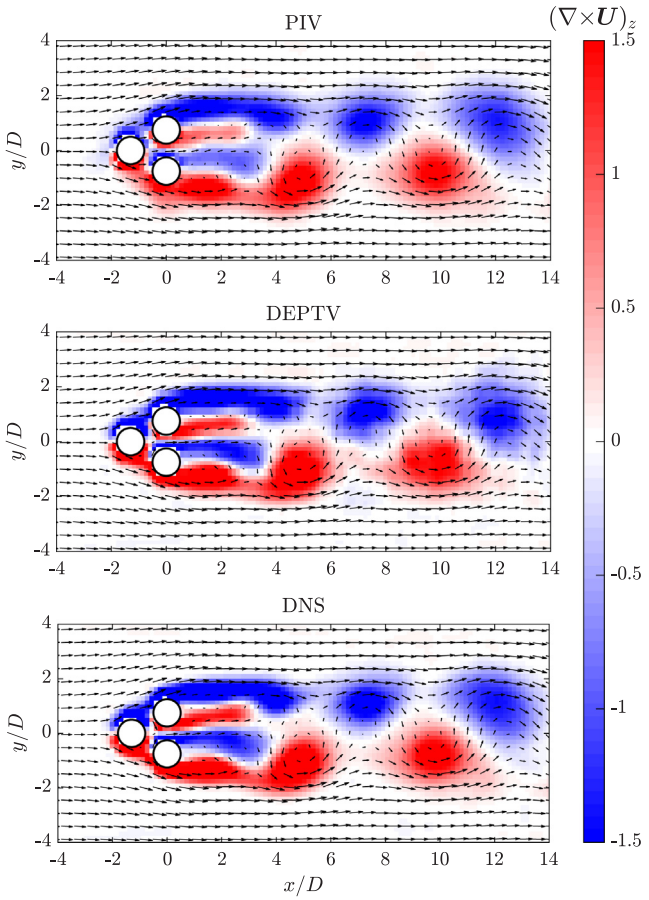

Fig. 10. Comparison of an instantaneous flow field for the fluidic pinball test case. $N_{ppp} = 0.01$, $b = 4$ pixels, $N_t = 5000$. Raw PIV data and reconstruction with 40 modes for DEPTV. DEPTV reconstruction is performed with $\boldsymbol{\Psi}_{PIV}$ obtained from a regular PIV in a coarse grid. The PIV vorticity is calculated in the same grid as the DEPTV in order to have a fair vorticity comparison.

here in a linear scale to make evident the differences in the first modes. The asymptotic behaviour is similar to the one observed in Fig. 4 (which was instead presented in logarithmic scale).

A comparison of an instantaneous flow field obtained with PIV and DEPTV for a bin size of 4 pixels is reported in Fig. 10. The out-of-plane vorticity is computed on the same grid for PIV, DEPTV and DNS to eliminate discrepancies due to truncation errors. The out-of-plane vorticity maps highlight that PIV can resolve the vorticity released in the far-wake since, after merging, the scales are sufficiently large with respect to the interrogation window. Nonetheless, some attenuation of the vorticity peaks is observed, due to a combination of amplitude modulation of the PIV processing.

In the near-wake and in the region around the cylinders, the performances of DEPTV are superior to those of standard PIV, with an excellent recovery of the vorticity in the shear layers and in the developing regions around the cylinders.

3.2.3. Reconstruction error

A quantitative comparison of the statistics of the reconstruction error for different bin sizes is reported in Fig. 11. The error is computed as in Eqs. 8 and 9.

The error map obtained for PIV is compared with:

- DEPTV on the full dataset (5000 snapshots) with bin size equal to 4, corresponding to 800 particles per bin on average;
- DEPTV on partial dataset (1000 snapshots) with bin size equal to 8, corresponding to 640 particles per bin on average;
- DEPTV on partial dataset (1000 snapshots) with bin size equal to 4, corresponding to 160 particles per bin on average.

The PIV error map highlights that the largest error is observed in the near wake and in the region close to the cylinders, where the flow characteristic scales are significantly smaller than the PIV interrogation window. In the far wake, due to the merging of the shedding wakes of the cylinders, the flow scales are larger, thus the bias errors due to finite spatial resolution are smaller.

Regarding DEPTV, using a smaller bin reduces the modulation error, especially in the region between the three cylinders and close to the cylinder surfaces. This is obtained at the expenses of the random error due to poor convergence of the ensemble particle modes if the number of particles per bin is not sufficiently large (see Fig. 11, bottom right). A good compromise should be found between the number of particles per bin and the bin size. Since the convergence of POD relates directly to second-order statistics, a reasonable criterion for the bin size is to have a number of particles per bin equal to the number of snapshots needed to achieve good convergence of the Reynolds stresses in an ensemble PTV approach. A general criterion is difficult to define, since indeed the convergence is dependent on the spectral richness of the flow.

To this purpose, a parametric study of the effect of the bin size and of the cut-off selection on the spatially-averaged error $\langle\hat{\varepsilon}_r\rangle$ is carried out. The error is evaluated in the full field and in the near field downstream of the pinball (i.e. $x/D \in [-2, 3]$, $y/D \in [-3, 3]$). For the parametric studies on the bin size, the DEPTV cut-off is always set to 40 modes for simplicity.

In the near field larger systematic error is expected due to finite spatial resolution, as already observed in Fig. 11, while in the far field random error are dominant.

The error $\langle\hat{\varepsilon}_r\rangle$ as a function of the normalized squared bin size is reported in Fig. 12. When considering the full field, the error reduction is limited since the resolution limits of PIV are affecting the measurement accuracy only in a small portion of the field. Since the random error is dominating in most of the domain, a large number of snapshots is required to improve the accuracy if compared to the PIV results. If a sufficiently large number of snapshots is available (for this test case $N_t > 2500$) an overall improvement is observed for a wide range of squared bin size (i.e. for $3 < b < 17$ pixels).

In the near field, the systematic error is dominant, thus DEPTV significantly outperforms the standard PIV process. For relatively-small bin size the systematic error of DEPTV is negligible; thus the error improves with an increasing number of snapshots. For instance, for the smallest bin size $b = 1$ pixel, the error scales approximately with the square root of the number of snapshots. For increasing bin size, a progressively larger share of error is due to finite spatial resolution, thus this improvement is less evident. For relatively large bin size, the systematic error is dominating, thus all curves collapse independently on the number of snapshots for the investigated range.

As observed in the previous test case, the selection of the number of modes for the reconstruction is critical to minimize the contamination of the reconstructed fields due to the introduction of modes with poor convergence. While for the cylinder wake the spectral compactness of the modal decomposition provided a trivial selection of the few significant modes, in this case, the fields exhibit wider spectral richness (see Fig. 9), thus posing the question of the most effective cut-off selection. In Fig. 13 the effect of the selection of the number of modes on the spatially-averaged error is investigated and compared to the error achieved by a low-order reconstruction based on the PIV fields and truncated with the same number of modes. In all cases it can be observed that it exists an optimum number of modes which minimizes the reconstruction error. This is a consequence of the convergence issues for higher-order modes, which carry a lower share of energy. For a fixed number of snapshots ($N_t = 1000$) increasing the bin size provides a slight improvement, displacing the optimum cut-off for the reconstruction to higher-order mode number. This is due to the reduction

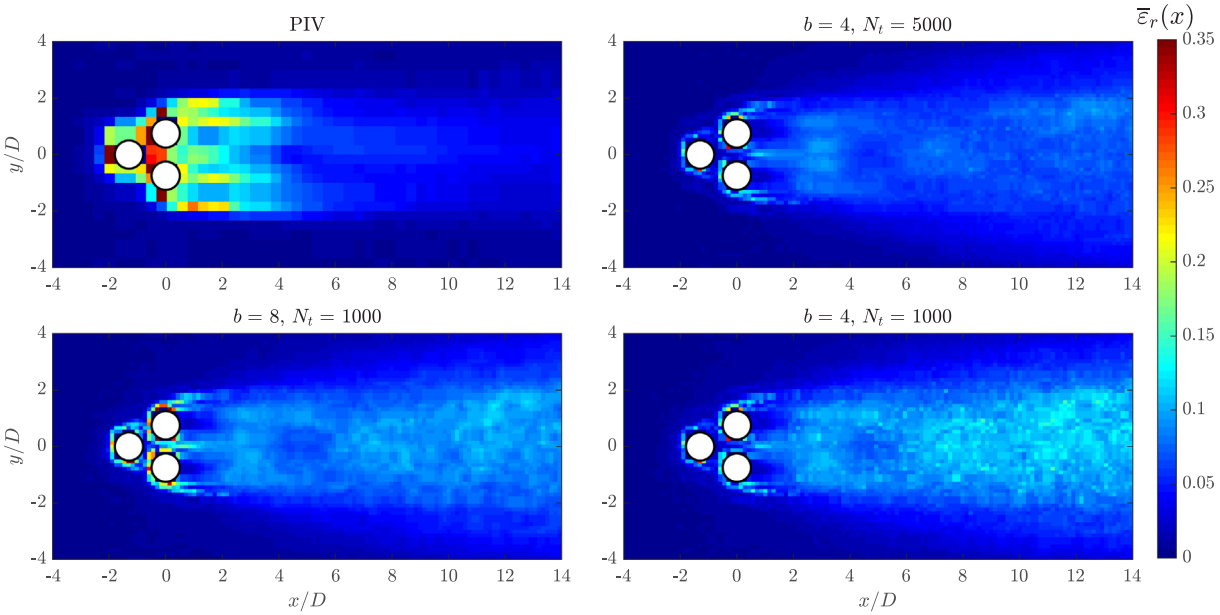

Fig. 11. Standard deviation of the error in the reconstructed flow fields for PIV (top left) and DEPTV with bin size of 4 with full dataset (top right) and bin size of 8 and 4 with only 1000 snapshots (bottom left and right, respectively). The error is normalized with the standard deviation of the velocity fluctuations of the DNS data. For the DEPTV cases the reconstruction is carried out with 40 modes.

of the random error; indeed doubling the linear bin size leads to 4 times more particles on average for each bin. At fixed bin size $b = 4$ pixels, the same effect is appreciated for an increasing number of samples (reduction of the minimum error and shift to the right of the minimum point). For the most energetic modes, there are no significant differences since 1000 snapshots are sufficient in this case to achieve satisfactory convergence.

In the near field, DEPTV significantly outperforms PIV thanks to the significant reduction of systematic errors due to the limited resolution. In this case, for fixed $N_t = 1000$, a significant reduction of the minimum error is observed when reducing the bin size, as well as of the error on the most energetic modes. This is a consequence of the dominance of the finite resolution errors in this part of the field. It can be also observed that, at fixed bin size, the error is weakly dependent on the number of snapshots, and is mostly defined by the bin size.

3.2.4. Setting the threshold

The problem in practical applications is that the curves of Fig. 13 are not available since, of course, the ground truth is unknown. The definition of an optimal threshold has been discussed in several recent works [33–35]. In this case, such methods are not of direct use since the high-resolution modes are *extended modes*, rather than the direct outcome of a Singular Value Decomposition. In this last case, the random error follows a Marchenko-Pastur distribution [35], while the high-order extended POD modes obtained with the DEPTV procedure reach asymptotically an energy level which depends on the measurement

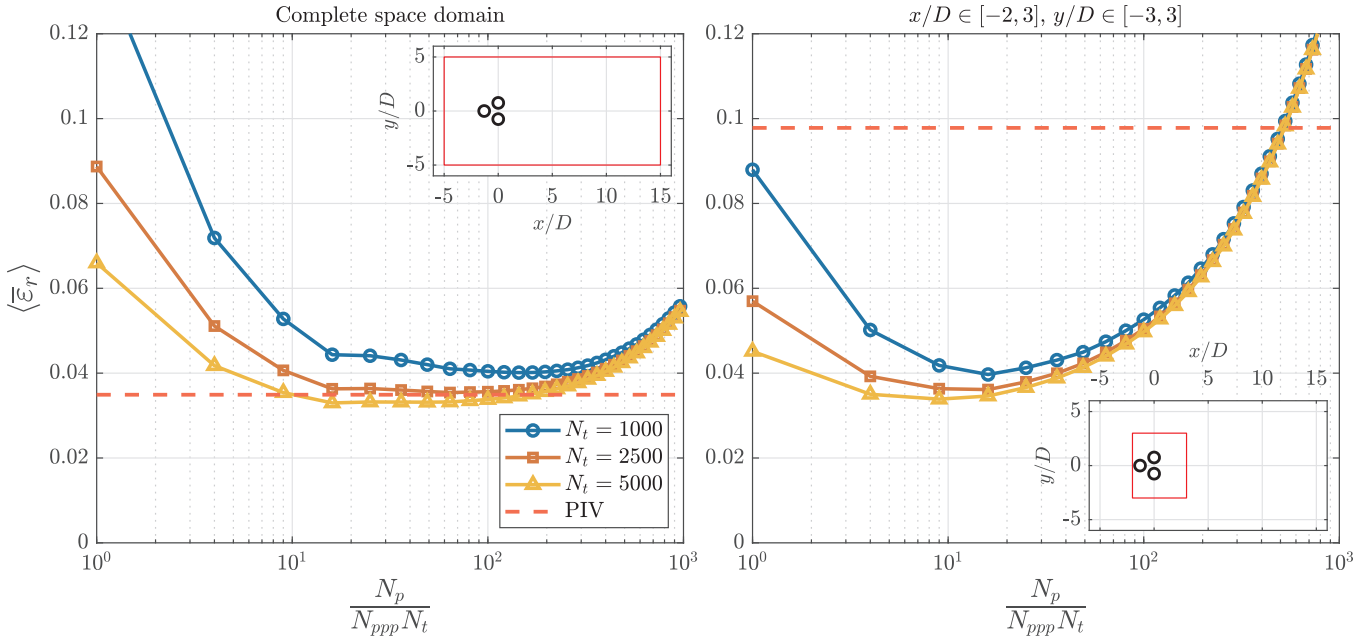

Fig. 12. Error on the velocity field as a function of the bin size. Error evaluated in complete space domain for figure in the left and in $x/D \in [-2, 3]$ and $y/D \in [-3, 3]$ for figure in the right, as indicated by the red rectangles within each plot. For DEPTV the cut-off is set to 40 modes for all cases.

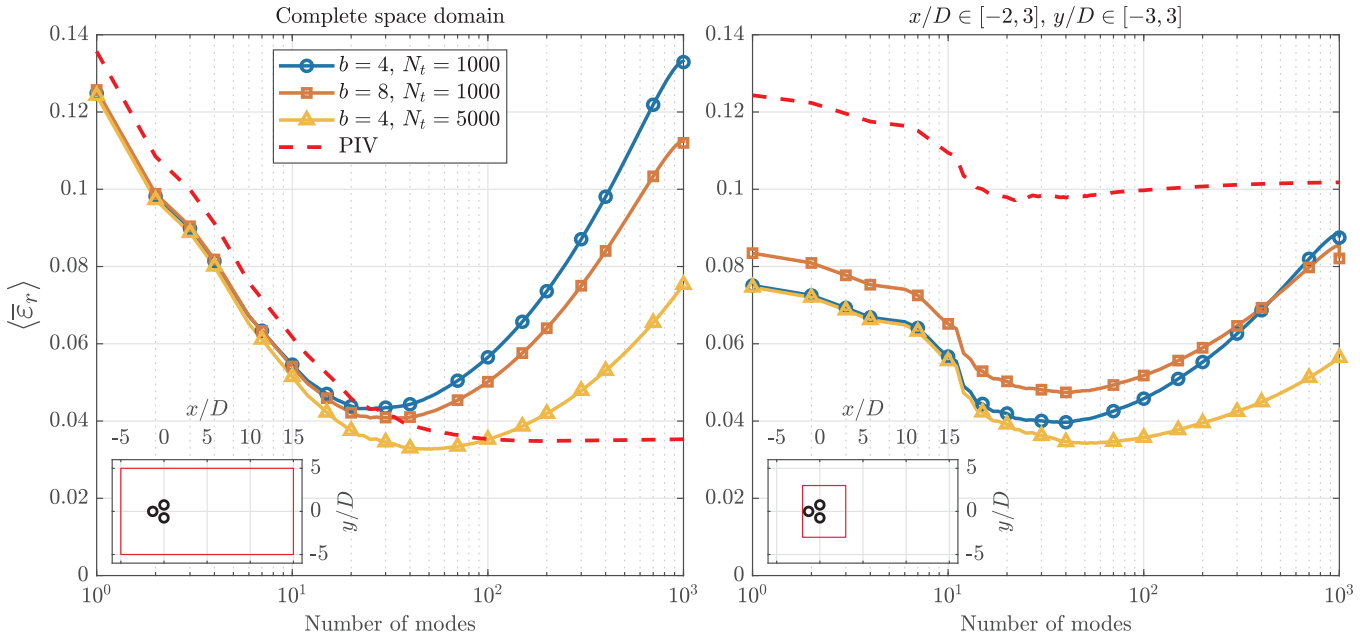

Fig. 13. Error in flow field as a function of the number of modes used in the reconstruction. Error evaluated in complete space domain for figure in the left and in $x/D \in [-2, 3]$ and $y/D \in [-3, 3]$ for the figure on the right, as indicated by the red rectangles within each plot. Markers are evenly distributed for representation purposes.

standard error, i.e. on the standard deviation of the velocity, divided by the square root of the number of particles in each bin [27]. This asymptotic value is thus a function of the noise level of the estimated modes and can be used to set an empirical threshold.

In Fig. 14 the error in the full field is reported as a function of the selected threshold. The cut-off is expressed in terms of the asymptotic value of the norm of the extended modes σ_∞ (which can be set as the norm of the highest order extended mode, or as an average of the highest order ones to reduce scatter). It can be observed that in all tested cases the spatially-averaged error exhibits a large plateau, which increases in size as convergence issues due to the random error are reduced (for instance increasing the bin size or the number of samples). The results in Fig. 14 suggest that the cut-off can be set by setting $1.1 < (\sigma_{cutoff}/\sigma_\infty)^2 < 3$ with minimal effect on the overall error.

4. Experimental validation

The experimental dataset used for the validation has been obtained from an experimental campaign carried out in the Göttingen-type wind tunnel of the Aerospace Engineering Research Group at the Universidad Carlos III de Madrid. The tunnel has a test section of $0.4 \times 0.4 \times 1.5$ m. The maximum wind tunnel speed is 20 m/s. The high-pass filtered free-stream turbulence intensity is below 0.5%.

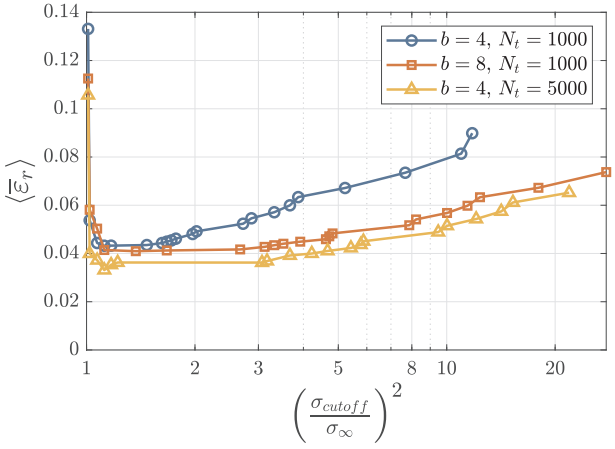

Fig. 14. Error on the velocity field as a function of energy level of last mode above the asymptotic value.

Two parallel cylinders, with a diameter equal to $D = 20$ mm and $d = 2$ mm respectively, are placed, with their centre located at the same streamwise location and with their axes orthogonal with respect to the freestream. The separation between the cylinder axes is equal to D. The experimental setup is sketched in Fig. 15.

As in the previous test cases, x and y indicate the streamwise and crosswise directions, respectively. The corresponding velocities are indicated with U and V, with lower-case letters corresponding to the respective velocity fluctuations. The origin of the coordinate system in the

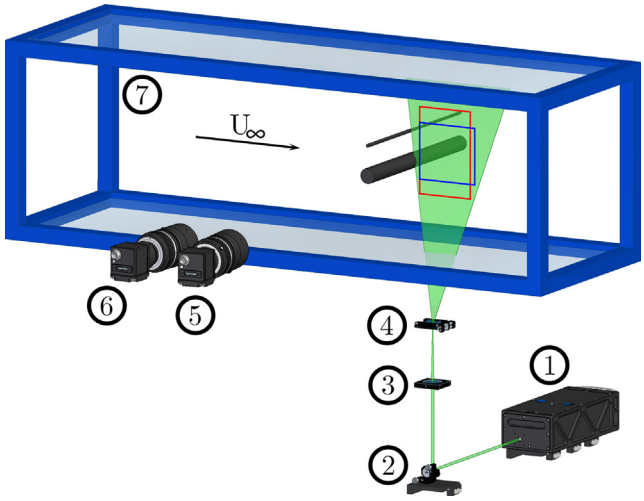

Fig. 15. Sketch of the experimental setup. (1) Laser (2) Mirror (3) Spherical lens (4) Cylindrical lens (5) Camera with 50 mm objective (6) Camera with 100 mm objective (7) Wind-tunnel test section. The red and blue rectangles indicate the field of view of cameras (5) and (6), respectively. (For interpretation of the references to colour in this figure legend, the reader is referred to the web version of this article.)

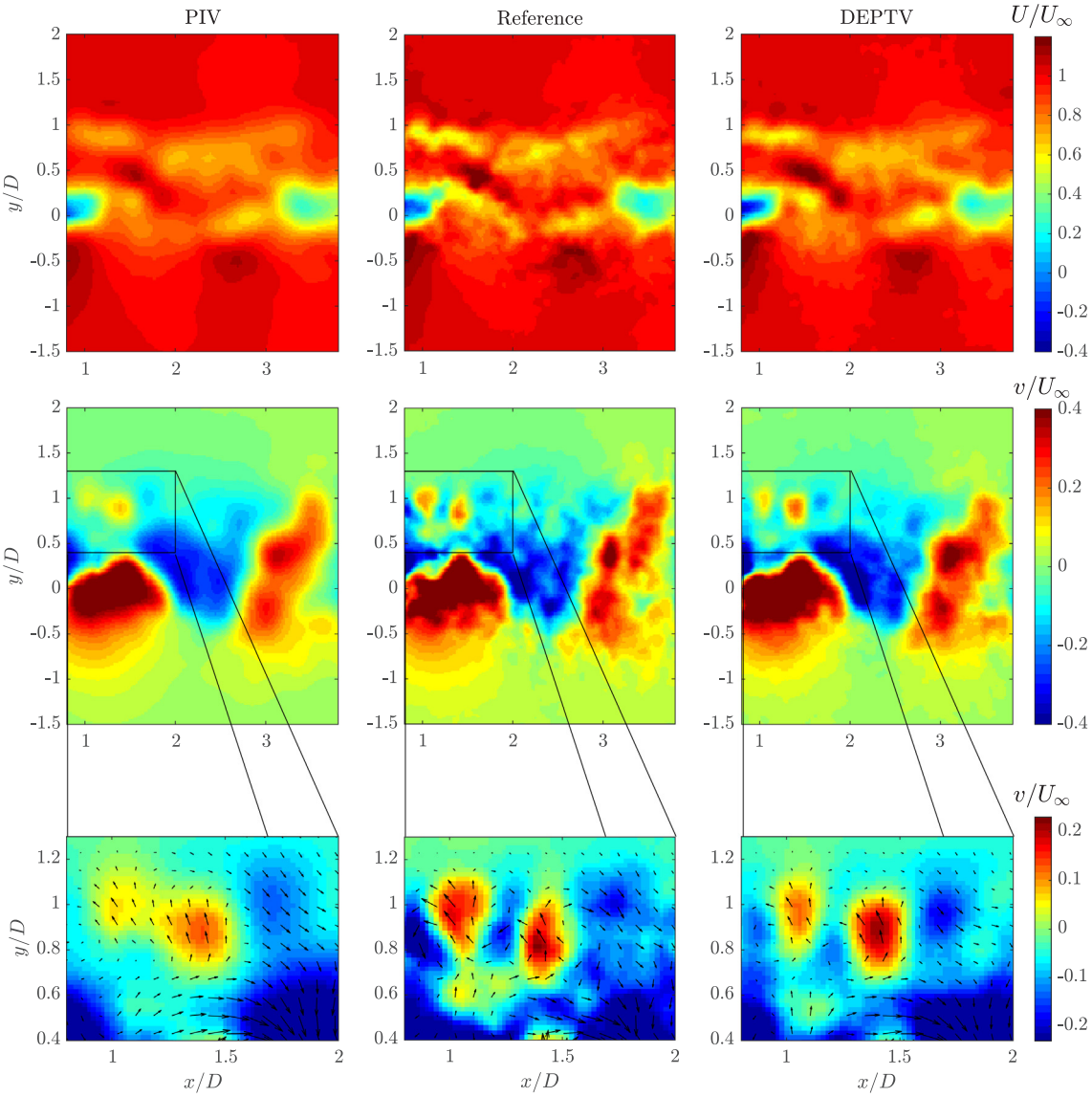

Fig. 16. Comparison of the instantaneous streamwise (top row) and crosswise (centre row) velocity components for PIV (left column) and DEPTV (right column) on the test camera, and PIV carried out on the reference cameras (center column). The bottom row contains insets of the crosswise velocity fields with superposed arrow vectors. The scale for the bottom row is changed to highlight differences.

streamwise direction is located in the centre of the cylinder section at the midplane of the test section.

Velocity-field measurements are carried out in the $x - y$ plane. Di-Ethyl-Hexyl-Sebacate (DEHS) droplets with ~ 1 μm diameter are generated with a Laskin nozzle and introduced upstream of the wind-tunnel settling chamber. A dual cavity Nd:Yag Quantel Evergreen laser (200 mJ/pulse at 15 Hz) with a cylinder and a spherical lens is used to produce a planar illumination with approximately 1 mm thickness in the measurement region.

Two *ANDOR Zyla sCMOS 5.5MP* cameras (2560 × 2160 pixel array, 6.5 × 6.5 μm pixel size) were used to capture PIV images. One camera is equipped with a Tokina objective with 50 mm focal length, with a resolution of about 10.3 pixels/mm and a magnification of approximately 0.067. This camera is used to carry out the PIV and the DEPTV processing and will be referred from now on as *test camera*. Owing to the achieved spatial resolution, for this camera the small cylinder diameter d is discretized with only approximately 20 pixels, while the large cylinder diameter D is discretized with about 200 pixels. It is thus to be expected that a standard PIV processing is not able to resolve the vortices shed in the wake of the small cylinder.

The second camera is equipped with a 100 mm focal-length Tokina objective, with a resolution of 22.6 pixels/mm and a magnification of about 0.147. This camera is used to build a reference field, owing to the larger resolution achieved.

The cameras capture particle images simultaneously, with the synchronization controlled by a Quantum composer 9520 Series Pulse Delay Generator. The time separation between the two lasers is set to 100 μs. The freestream velocity is set to 5.2 m/s, thus resulting in a displacement of approximately 5.3 and 11.8 pixels on the test camera and the reference camera, respectively.

An ensemble of 1300 snapshots was acquired for both cameras. A larger dataset of 12000 snapshots was captured with the test camera to improve the convergence of the DEPTV method. The particle images of both datasets have been pre-processed with the POD-based approach proposed by Mendez et al. [36].

The PIV image analysis was carried out with the same multi-grid multi-pass code described in Section 3.2. The final interrogation window is set to 64 × 64 pixels with 75% overlap for both the test camera and the reference cameras. This is equivalent to 6.2 × 6.2 mm for the test camera, and 2.9 × 2.9 mm for the reference camera.

It is important to remark that, since the cameras capture simultaneously, the resolution limit for standard PIV is related to the mean particle spacing for both cameras. For this reason, an artificially large interrogation window is used for the test camera to guarantee a resolution gain when using the reference camera. The particle image density is indeed set to 0.01 particles per pixel on the test camera, thus resulting in about 8 and 40 particles per interrogation window for the reference and test camera, respectively. The reference camera thus reaches higher spatial resolution at the expense of higher sensitivity to noise. For this reason, it will be considered as a reference only for statistics assessment and not for direct instantaneous field comparison. Even if for the present test case it is not available a fully-trustworthy ground truth, it has to be noted here that the present section is aimed at assessing that the proposed methodology provides reliable results in presence of real experimental data. While the synthetic test cases allow characterizing in detail the performance of the method, real imaging and measurement noise conditions are used to test the proposed method.

DEPTV is carried out with bins of 16×16 pixels with 50% overlap, thus aiming at an increase of the spatial resolution of a factor of 4.

A calibration target with black dots on a white background is used to project the images of the two cameras onto the same world coordinate system. The laser sheet position is identified with a stereoscopic self-calibration [37]. This allows direct comparison between the test and reference results and reduces the systematic errors on the magnification measurement [38].

A comparison of the instantaneous streamwise and crosswise velocity fields obtained by standard PIV on the test and reference cameras, and with DEPTV on the test camera is reported in Fig. 16. The results are presented in non-dimensional form using the large-cylinder diameter D and the freestream velocity U_∞ as reference length and velocity scales, respectively. The wake of the largest cylinder is captured with reasonable accuracy by the standard PIV, with weak smoothing if compared to the reference and the DEPTV fields. Larger differences are observed in the wake of the smallest cylinder, in particular for what concerns both the streamwise momentum defect (underestimated by the standard PIV process) and the strong attenuation of the vortices shed in the wake. This is particularly evident from the observation of the contour plots of the crosswise velocity component (bottom row of Fig. 16).

A quantitative comparison is carried out in terms of a streamwise spectrum of the crosswise velocity fluctuations for $y/D = 0.95$ (see Fig. 17), where the shedding signature of the small cylinder should be observed. The frequency range is presented in a non-dimensional form with the Strouhal number St based on the diameter of the small cylinder and on the freestream velocity. Considering that the Reynolds number based on the small cylinder diameter is ≈ 700, the wake Strouhal number for an isolated circular cylinder would be about 0.2 [39].

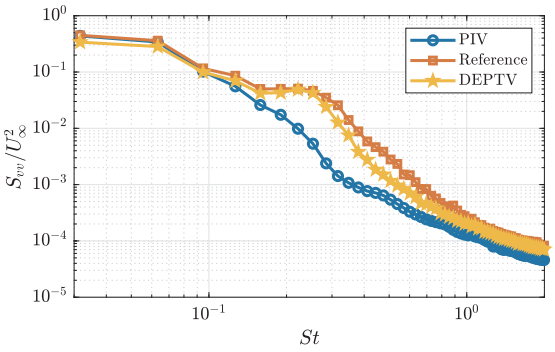

Fig. 17. Streamwise spectra of the crosswise velocity fluctuations.

The attenuation of the crosswise velocity fluctuations for the standard PIV is observed in the streamwise spectrum. The expected peak, detected in the reference at higher resolution, is not present in the spectrum of the low-resolution PIV data. This is not surprising since the size of the interrogation window (about 3.5 times the diameter of the smallest cylinder) corresponds to spectral cutoff at $St = 0.29$. It is well-known, however that modulation effects start being significant at scales above the interrogation window size for a standard PIV approach [40]. If considering a standard cross-correlation without weighting windows, the Modulation Transfer Function of the PIV process is a *sinc* function, with attenuation of almost 40% already at a scale twice as large at the interrogation window. This explains why the spectrum of the standard PIV departs from the reference one already at $St \approx 0.15$.

DEPTV can maintain a spectral behaviour similar to the reference up to a Strouhal number of almost 0.3, thus resulting in a significant improvement of the dynamic spatial range.

5. Conclusions

A novel method to enhance the resolution of sparse particle-based measurements has been proposed. The working principle is based on exploiting the concept of Ensemble Particle Tracking Velocimetry and enforcing it to the estimation of POD modes. The high-resolution POD modes are then used to estimate high-resolution velocity fields. While the proposed method does not enforce sparsity (such as the $\mathscr{L}^1$-norm minimization problem), the reconstruction of the high-resolution signal from sparse measurements leverages on principles similar to those of compressed sensing. The main novelty is that a high-resolution dictionary is not available beforehand and is constructed directly using the PIV snapshots and the particle images. This gives the method great flexibility for application to experimental data also in innovative configurations where benchmarks are not available.

The following remarks arise from the analysis of the results:

- The method is based on performing a projection on the temporal basis obtained by PIV. As a consequence, flow features that are captured by PIV but attenuated (because of a size comparable to the interrogation window) can be recovered with theoretically null attenuation. Flow features that are completely cancelled out by the PIV process (because much smaller than the PIV interrogation window size, or even below the mean particle spacing) can be recovered if some degree of correlation exists with any of the large scales that are properly captured. This often happens in turbulent flows and is a direct consequence of the turbulence cascade. Nonetheless, if the correlation is weak, this recovery process might be more difficult.
- The convergence of the process requires a relatively-large number of samples, as typical for the EPTV process used for the estimation of the mean flow field and flow statistics. As a good rule of thumb, since POD is based on second-order statistics, the number of samples to be captured should be sufficient to achieve sufficient convergence of the Reynolds stresses at the EPTV resolution (see Ref. [13] for the assessment of such convergence). To apply this approach, the process should be statistically stationary. A future line of development is the extension of the method to statistically-unsteady flows.
- High-energy modes require fewer samples to converge, as typical in POD processing. As a consequence, the method shows its full potential in flows with clear separation of scales and spectral signature, i.e. which can be represented with a compact subset of POD modes. This should be taken into account if considering the application of the method to spectrally-richer turbulent flows.
- The lack of convergence of the *ensemble particle modes* results in significant levels on noise into these modes. The mode norm profile, however, shows an asymptotic behaviour and it is suggested herein to truncate the low-order reconstruction to the mode whose squared norm is 20–100% larger than the asymptotic value.

As a general remark, this is in the author's knowledge the first self-tunable compressed-sensing algorithm for high-resolution particle-based field measurements. Sample code for the cylinder test is available on GitHub: https://github.com/StefanoDiscetti/DEPTV.

CRediT authorship contribution statement

J. Cortina-Fernández: Software, Validation, Investigation, Visualization, Data curation, Writing - original draft, Writing - review & editing. **C. Sanmiguel Vila:** Validation, Investigation, Writing - review & editing. **A. Ianiro:** Conceptualization, Methodology, Resources, Supervision, Writing - original draft, Writing - review & editing, Funding acquisition. **S. Discetti:** Conceptualization, Methodology, Resources, Supervision, Software, Validation, Visualization, Investigation, Data curation, Writing - original draft, Writing - review & editing, Funding acquisition.

Declaration of Competing Interest

The authors declare that they have no known competing financial interests or personal relationships that could have appeared to influence the work reported in this paper.

Acknowledgements

CSV, SD and AI were partially supported by the Grant DPI2016-79401-R funded by the Spanish State Research Agency (SRA) and European Regional Development Fund (ERDF). The authors warmly acknowledge N. Deng, B. Noack, M. Morzynski and L. Pastur for providing the dataset of the fluidic pinball.

References

[1] J. Westerweel, G.E. Elsinga, R.J. Adrian, Particle Image Velocimetry for Complex and Turbulent Flows, Annu. Rev. Fluid Mech. 45 (2013) 409–436.
[2] M. Raffel, C.E. Willert, F. Scarano, C.J. Kähler, S.T. Wereley, J. Kompenhans, Particle Image Velocimetry: A Practical Guide, Springer, 2018.
[3] B. Fond, C. Abram, F. Beyrau, On the characterisation of tracer particles for thermographic particle image velocimetry, Appl. Phys. B 118 (2015) 393–399.
[4] S. Abe, K. Okamoto, H. Madarame, The development of PIV–PSP hybrid system using pressure sensitive particles, Meas. Sci. Technol. 15 (2004) 1153–1157.
[5] R.J. Adrian, Dynamic ranges of velocity and spatial resolution of particle image velocimetry, Meas. Sci. Technol. 8 (1997) 1393–1398.
[6] S. Discetti, F. Coletti, Volumetric velocimetry for fluid flows, Meas. Sci. Technol. 29 (2018) 042001.
[7] S. Pope, Turbulent Flows, Cambridge University Press, 2000.
[8] C.J. Kähler, T. Astarita, P.P. Vlachos, J. Sakakibara, R. Hain, S. Discetti, R. La Foy, C. Cierpka, Main results of the 4th international PIV challenge, Exp. Fluids 57 (2016) 97.
[9] J. Westerweel, P. Geelhoed, R. Lindken, Single-pixel resolution ensemble correlation for micro-PIV applications, Exp. Fluids 37 (2004) 375–384.
[10] S. Scharnowski, R. Hain, C.J. Kähler, Reynolds stress estimation up to single-pixel resolution using PIV-measurements, Exp. Fluids 52 (2012) 985–1002.
[11] E. Cowen, S. Monismith, A hybrid digital particle tracking velocimetry technique, Exp. Fluids 22 (1997) 199–211.
[12] C.J. Kähler, S. Scharnowski, C. Cierpka, On the resolution limit of digital particle image velocimetry, Exp. Fluids 52 (2012) 1629–1639.
[13] N. Agüera, G. Cafiero, T. Astarita, S. Discetti, Ensemble 3D PTV for high resolution turbulent statistics, Meas. Sci. Technol. 27 (2016) 124011.
[14] C. Sanmiguel Vila, R. Örlü, R. Vinuesa, P. Schlatter, A. Ianiro, S. Discetti, Adverse-pressure-gradient effects on turbulent boundary layers: statistics and flow-field organization, Flow Turbul. Combust. 99 (2017) 589–612.
[15] J.H. de Baar, M. Percin, R.P. Dwight, B.W. van Oudheusden, H. Bijl, Kriging regression of PIV data using a local error estimate, Exp. Fluids 55 (2014) 1650.
[16] R. Everson, L. Sirovich, Karhunen-Loeve procedure for gappy data, J. Opt. Soc. Am. A 12 (1995) 1657–1664.
[17] D. Venturi, G.E. Karniadakis, Gappy data and reconstruction procedures for flow past a cylinder, J. Fluid Mech. 519 (2004) 315–336.
[18] S.G. Raben, J.J. Charonko, P.P. Vlachos, Adaptive gappy proper orthogonal decomposition for particle image velocimetry data reconstruction, Meas. Sci. Technol. 23 (2012) 025303.
[19] N.E. Murray, L.S. Ukeiley, An application of gappy pod, Exp. Fluids 42 (2007) 79–91.
[20] N. Deng, L.R. Pastur, M. Morzyński, B.R. Noack, Route to chaos in the fluidic pinball, in: ASME 2018 5th Joint US-European Fluids Engineering Division Summer Meeting, Am. Soc. Mech. Eng. V001T01A005.
[21] N. Deng, B.R. Noack, M. Morzyński, L.R. Pastur, Low-order model for successive bifurcations of the fluidic pinball, J. Fluid Mech. 884 (2020) A37.
[22] L. Sirovich, Turbulence and the dynamics of coherent structures. II. Symmetries and transformations, Q. Appl. Math. 45 (1987) 573–582.
[23] J. Kutz, S. Brunton, B. Brunton, J. Proctor, Dynamic Mode Decomposition, Society for Industrial and Applied Mathematics, Philadelphia, PA, 2016.
[24] K. Taira, T. Colonius, The immersed boundary method: A projection approach, J. Comput. Phys. 225 (2007) 2118–2137.
[25] T. Colonius, K. Taira, A fast immersed boundary method using a nullspace approach and multi-domain far-field boundary conditions, Comput. Methods Appl. Mech. Eng. 197 (2008) 2131–2146.
[26] J. Borée, Extended proper orthogonal decomposition: a tool to analyse correlated events in turbulent flows, Exp. Fluids 35 (2003) 188–192.
[27] J.F. Kenney, E.S. Keeping, Mayhematics of Statistics, part II, second ed., D. van Nostrand Company Inc, Toronto, New York, London, 1951.
[28] L.R. Pastur, N. Deng, M. Morzyński, B.R. Noack, Reduced-order modeling of the fluidic pinball, in: Chaotic Modeling and Simulation International Conference, Springer, pp. 205–213.
[29] J. Soria, An investigation of the near wake of a circular cylinder using a video-based digital cross-correlation particle image velocimetry technique, Exp. Thermal Fluid Sci. 12 (1996) 221–233.
[30] F. Scarano, Iterative image deformation methods in PIV, Meas. Sci. Technol. 13 (2001) R1.
[31] T. Astarita, Analysis of velocity interpolation schemes for image deformation methods in PIV, Exp. Fluids 45 (2008) 257–266.
[32] R.D. Keane, R.J. Adrian, Y. Zhang, Super-resolution particle imaging velocimetry, Meas. Sci. Technol. 6 (1995) 754–768.
[33] M. Gavish, D.L. Donoho, The optimal hard threshold for singular values is $4/\sqrt{3}$, IEEE Trans. Inf. Theory 60 (2014) 5040–5053.
[34] M. Raiola, S. Discetti, A. Ianiro, On PIV random error minimization with optimal pod-based low-order reconstruction, Exp. Fluids 56 (2015) 75.
[35] B.P. Epps, E.M. Krivitzky, Singular value decomposition of noisy data: noise filtering, Exp. Fluids 60 (2019) 126.
[36] M. Mendez, M. Raiola, A. Masullo, S. Discetti, A. Ianiro, R. Theunissen, J.-M. Buchlin, Pod-based background removal for particle image velocimetry, Exp. Thermal Fluid Sci. 80 (2017) 181–192.
[37] B. Wieneke, Stereo-PIV using self-calibration on particle images, Exp. Fluids 39 (2005) 267–280.
[38] S. Discetti, R.J. Adrian, High accuracy measurement of magnification for monocular PIV, Meas. Sci. Technol. 23 (2012) 117001.
[39] J.H. Lienhard, et al., Synopsis of lift, drag, and vortex frequency data for rigid circular cylinders, volume 300, Technical Extension Service, Washington State University, 1966.
[40] T. Astarita, Adaptive space resolution for PIV, Exp. Fluids 46 (2009) 1115.